



First-principle calculation investigation of NbMoTaW based refractory high entropy alloys

Y.L. Hu^a, L.H. Bai^a, Y.G. Tong^{a,*}, D.Y. Deng^b, X.B. Liang^c, J. Zhang^a, Y.J. Li^d, Y.X. Chen^c

^a College of Automobile and Mechanical Engineering, Changsha University of Science and Technology, Changsha, China

^b College of Materials Science and Engineering, Changsha University of Science and Technology, Changsha, China

^c National Institute of Defense Technology Innovation, Academy of Military Sciences PLA China, Beijing, China

^d Hunan Key Laboratory of Super Microstructure and Ultrafast Process, School of Physics and Electronics, Central South University, Changsha, China

ARTICLE INFO

Article history:

Received 15 November 2019

Received in revised form

19 January 2020

Accepted 20 January 2020

Available online 1 February 2020

Keywords:

High entropy alloys

First-principle calculation

Phase structure

Elastic properties

Electronic structure

ABSTRACT

Alloying is an effective method to strengthen high entropy alloys (HEAs). Unfortunately, most of the investigations focus on the perspective of experiments and few are available from the perspective of atomic and electrical scale such as electronic structure, energy band structure and charge density. In present work, first-principle calculation based on density functional theory was employed to calculate the ground state total energy, lattice parameters, elastic constants and polycrystal modulus of NbMoTaW and NbMoTaWV refractory high entropy alloys (RHEAs). The effects of V addition on the phase structure, elastic properties and electronic structure of NbMoTaW-based RHEAs were studied, respectively. V addition is helpful to improve the mechanical properties of NbMoTaW alloy according to the calculated value of shear modulus to bulk modulus, Cauchy pressure and Vickers hardness. Based on calculated energy band, electronic state density, charge density and charge density difference, V addition is found to shorten the pseudo-energy gap and enhance interaction force between Mo and W atoms. This tends to improve the mechanical properties of the alloy. The calculated results were in good agreement with the experimental data, demonstrating that the methods were effective in predicting the performance of RHEAs.

© 2020 Elsevier B.V. All rights reserved.

1. Introduction

High entropy alloys (HEAs) [1], as well as named as multi-principal component alloy, is a new type of superalloy, which are composed of five or more elements with equal or near equal atomic ratio. Unlike the predicted results by traditional alloy theory and Gibbs phase law, HEAs do not form multiphase compounds which weaken the properties of materials for existing many elements. On the contrary, because the high entropy effect hinders the formation of brittle phases such as intermetallic compounds, HEAs show excellent “collective characteristics” [2]. Compared with the traditional alloys, HEAs have single-phase BCC, FCC or HCP structure, attracting extensive attentions for their high strength, high hardness, high wear resistance, excellent high temperature oxidation resistance, corrosion resistance, superior thermal stability and other comprehensive properties [3–7]. In particular, refractory high

entropy alloys (RHEAs), constituted of refractory elements such as Nb, Ta, Mo, W, are considered to be new superalloys for high temperature applications because of their superior mechanical strength at elevated temperatures compared with Ni-based alloys and Ni₃Al-based intermetallic and other superalloys [8,9]. They have broad potential applications as a structural material in aviation, aerospace, metallurgy, nuclear energy and other fields of high temperature resistance due to their high melting points (above 2000 °C), high strength and excellent high temperature resistance [10].

The newly Mo₂₅Nb₂₅Ta₂₅W₂₅ RHEA, which is completely composed of refractory metal elements, has been reported for the first time by Senkov in 2010 [11]. The compressive strength of Mo₂₅Nb₂₅Ta₂₅W₂₅ RHEA is 1211 MPa at room temperature and 405 MPa at 1600 °C, respectively. Importantly, it still has a stable single-phase BCC structure at 1400 °C. The surprised results demonstrate that it is a new type of high temperature structural material for its excellent high temperature resistance and high temperature strength. To meet the increasing demand for high performance structural materials in high temperature applications,

* Corresponding author.

E-mail address: tongyonggang_csust@163.com (Y.G. Tong).

it is of great significance to further improve the mechanical properties of $\text{Mo}_{25}\text{Nb}_{25}\text{Ta}_{25}\text{W}_{25}$ RHEA. Alloying is an effective and common method to improve the mechanical properties of alloys. For example, Wang et al. found that Al addition resulted in the formation of BCC structure and hardened $\text{Al}_x\text{CoCrFeNi}$ high entropy alloys [12]. Salishchev et al. found V addition could improve significantly CoCrFeNi -based high entropy alloy's hardness from 160 Hv to 524 Hv and the compressive yield strength from $\sigma_{0.2} = 190$ MPa–1435 MPa [13]. Especially, V addition was demonstrated to be effectively improve the mechanical properties of NbMoTaW RHEA such as improving the compressive yield strength from $\sigma_{0.2} = 1058$ MPa–1246 MPa based on the experiments [11]. Xin et al. prepared single-phase nanocrystalline (NC) refractory VNbMoTaW HEAs and found its hardness reaches 11.4 GPa at 1150 °C [14]. Unfortunately, as far as we know, most of the research about NbMoTaW RHEA are focusing on experiments. There are few theoretical calculations to reveal the alloying mechanical strengthening of NbMoTaW RHEA. No publish information is available on performances enhancement from the perspective of atomic and electrical scale such as electronic structure, band structure and charge density.

First-principles, as an effective and economic calculational tool, is widely employed to predict material properties from atomic scale. In this work, the crystal model of NbMoTaW and NbMoTaWV RHEA were built based on virtual crystal approximate method (VCA) [15–18] and special quasi-random supercell method (SQS) [19]. The ground total energy, phase structure, mechanical properties as well as electronic structure including the band structure, electronic density of states, charge density and charge density difference were systematically calculated to reveal the effects of V alloying on the properties of NbMoTaW-based RHEA. In addition, the similarities and differences of these methods including VCA and SQS in the computational accuracy and performance prediction for disordered high entropy alloys were compared.

2. Methods

2.1. Theoretical methods and calculation models

Fig. 1 is the unoptimized VCA model and SQS supercell model of NbMoTaW and NbMoTaWV RHEA, respectively. In this work, a series of supercell model containing 4, 10, 20 and 10 atoms were built, and they were expanded to $1 \times 1 \times 2$ and $1 \times 1 \times 5$ on the basis of a single cell. All the calculations were performed using CASTEP module, which depended on the first-principle plane-wave pseudopotential method based on density functional theory (DFT). The crystal models were respectively established by VCA and SQS methods. The electronic exchange-correlation terms were described using Generalized Gradient Approximation (GGA) and Perdew Burke Ernzerhof (PBE) function. Norm conserving pseudopotential for all the elements in reciprocal space were applied. The valence electrons of all the elements are Nb $4d^45s^1$, Mo $4d^5s^1$, Ta $5d^36s^2$, W $5d^46s^2$, and V $3d^34s^2$. The cutoff energy (E_{cut}) of plane and special k-points sampling integration over the Brillouin zone were adopted using Monkhorst-Pack method according to the system defaults corresponding to fine-quality. Namely, E_{cut} was set to be 450 eV. K-point meshes of different models were set to be $8 \times 8 \times 4$ for BCC NbMoTaW, $8 \times 8 \times 2$ for BCC NbMoTaWV, $6 \times 6 \times 1$ for FCC NbMoTaWV, $10 \times 10 \times 1$ for HCP NbMoTaWV and $8 \times 8 \times 8$ for BCC NbMoTaWV built by VCA method, respectively. Partially, the k-point mesh was set to be $8 \times 8 \times 3$ during the elastic constant calculation of the SQS supercell model. The structure optimization of above models adopted Broyden Fletcher Goldfarb Shanno (BFGS) scheme. The maximal geometry optimization iterations step is 100. Pulay density mixing method was used in self-consistent calculation (SCF). The self-consistent convergence conditions were as follows: the total energy was 1×10^{-5} eV/atom, the force less than 0.03 eV/Å, the tolerance displacement less than 0.001 Å, and the stress less than 0.05 GPa. The single-point energy,

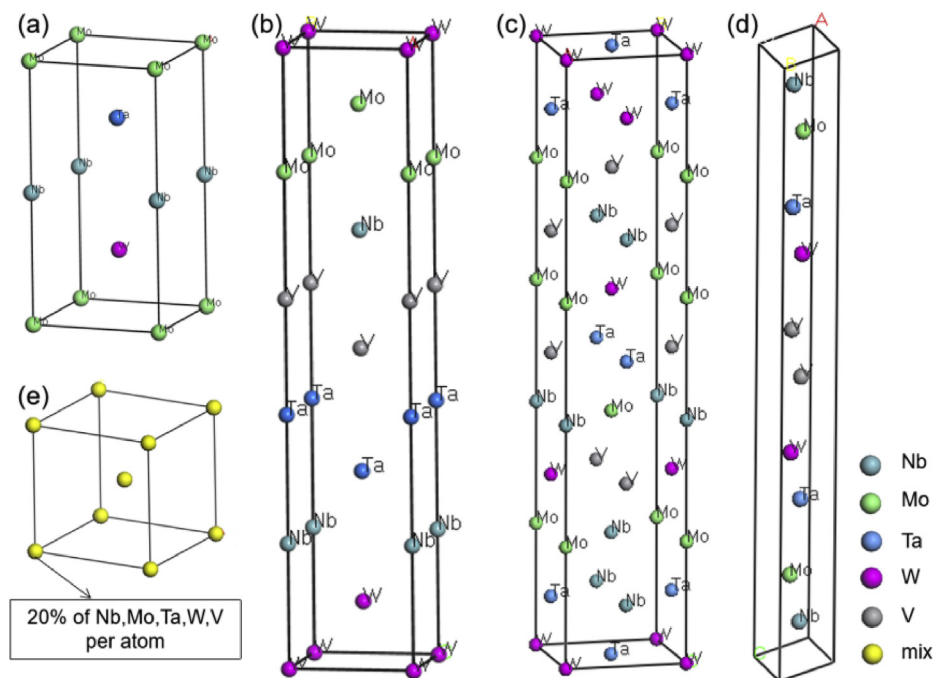


Fig. 1. Unoptimized SQS supercell model and VCA model. (a) BCC NbMoTaW of $1 \times 1 \times 2$; (b) BCC NbMoTaWV of $1 \times 1 \times 5$; (c) FCC NbMoTaWV of $1 \times 1 \times 5$; (d) HCP NbMoTaWV of $1 \times 1 \times 5$; (e) BCC NbMoTaWV built by VCA.

elastic and electronic properties of all the models were finally calculated after cell optimization.

In order to verify the accuracy of the above parameters, the lattice parameters of single-phase BCC NbMoTaW RHEA was calculated to be 3.193 Å, which was well agreed with the calculated value (3.271 Å) by Li [20] and the experimental value (3.213 Å) by Senkov [21]. It is demonstrated that the above parameters during calculations are reasonable.

3. Experimental

NbMoTaW and NbMoTaWV RHEA were prepared by vacuum arc melting after equimolar mixing corresponding elements with a purity of 99.9 wt%. Before melting, the furnace was vacuumed to 3×10^{-3} Pa and then, high purity argon gas was injected into the furnace. The alloy ingots were repeatedly melted 5 times to ensure the uniformity of their composition and structure. The specimens were cut from the ingots using wire electrical discharge machining. The structures of the samples were characterized by X-ray diffraction (XRD, Rigaku D/Max 2550VB-) using Cu K α radiation at a scanning rate of 5°/min and scanning from $2\theta = 20^\circ$ – 90° . Microhardness of the alloys was measured by Vickers hardness tester. Getting an average value among three different points under 100 g for 15s.

4. Results and discussion

4.1. Phase structure

Normally, the empirical criterions are used to predict the phase structure of RHEA. According to the literatures [22], when the average valence electron concentration (VEC) is larger than 8, FCC phase is stable. If $VEC < 6.87$, BCC phase is stable. BCC and FCC phase coexist between 6.87 and 8. Besides, atomic size difference ($\delta < 6.6\%$) is considered as a single-phase BCC solid solution. The values of VEC and δ for NbMoTaWV RHEA calculated using the empirical criterions are 5.463 (< 6.87) and 3.20% ($< 6.6\%$), respectively, indicating that the NbMoTaWV RHEA is a single-phase BCC structure.

Table 1 shows the formation enthalpy (E_{form}) and cohesive energy (E_{coh}) calculated based on the optimized SQS model of NbMoTaWV RHEA. Table 2 shows the total energy (E_{solid}) of a single cell for every component in NbMoTaWV RHEA and total energy (E_{atom}) of individual atom in a corresponding single cell, respectively. Formation enthalpy plays a crucial role to characterize the ability of forming metal compounds. Generally speaking, the more negative formation enthalpy is liable to form metal compounds. The cohesive energy is used to determine the stability of the crystal. The lower the cohesive energy, the more stable the crystals [23]. The E_{form} and E_{coh} of NbMoTaWV RHEA were respectively calculated based on formula (1) and (2):

$$H_{\text{form}} = \frac{1}{a+b+c+d+e} (E_{\text{tot}} - aE_{\text{solid}}^{\text{Nb}} - bE_{\text{solid}}^{\text{Mo}} - cE_{\text{solid}}^{\text{Ta}} - dE_{\text{solid}}^{\text{W}} - eE_{\text{solid}}^{\text{V}}) \quad (1)$$

$$E_{\text{coh}} = \frac{1}{a+b+c+d+e} (E_{\text{tot}} - aE_{\text{atom}}^{\text{Nb}} - bE_{\text{atom}}^{\text{Mo}} - cE_{\text{atom}}^{\text{Ta}} - dE_{\text{atom}}^{\text{W}} - eE_{\text{atom}}^{\text{V}}) \quad (2)$$

In the formula (1) and (2), E_{tot} is the total energy of optimized NbMoTaWV RHEA SQS model. a , b , c , d and e represent the atomic numbers of Nb, Mo, Ta, W and V in the corresponding crystal cell, respectively. $E_{\text{solid}}^{\text{Nb}}$, $E_{\text{solid}}^{\text{Mo}}$, $E_{\text{solid}}^{\text{Ta}}$, $E_{\text{solid}}^{\text{W}}$, $E_{\text{solid}}^{\text{V}}$ are the total energy of a single crystal cell for every component in

NbMoTaWV RHEA and $E_{\text{atom}}^{\text{Nb}}$, $E_{\text{atom}}^{\text{Mo}}$, $E_{\text{atom}}^{\text{Ta}}$, $E_{\text{atom}}^{\text{W}}$, $E_{\text{atom}}^{\text{V}}$ are the total energy of individual atom in a corresponding single crystal cell, respectively. From the data in Table 1, we can see that both E_{form} and E_{coh} of BCC NbMoTaWV RHEA are negative. There is a slight difference of E_{coh} among BCC, FCC, and HCP. BCC structure with more negative E_{form} and E_{coh} will be formed in the first time. The calculated data indicates that NbMoTaWV RHEA is single-phase BCC structure.

In order to further analyze the phase structure of NbMoTaWV RHEA, the theoretical XRD spectrum of the NbMoTaW and NbMoTaWV RHEA from $2\theta = 20^\circ$ – 90° were calculated using Powder Diffraction in Material Studio's Reflex module. Fig. 2 shows the theoretical and experimental XRD spectrums of both RHEA in this work. It is obviously observed that the strong peak positions in calculated XRD spectrum using VCA and SQS methods are well consistent with the experimental results, which indicates that NbMoTaW and NbMoTaWV RHEA formed a single-phase BCC solid solution. Besides, neutron diffraction patterns of both RHEA were measured and also exhibited a single-phase BCC solid solution [11], which were well agreed with our experimental and calculated results. Interestingly, the tendency of strong peak moving to the high angle demonstrated that the lattice parameters of NbMoTaWV RHEA reduced after the addition of V atom with relatively small atomic size.

The calculated lattice parameters of NbMoTaW and NbMoTaWV RHEA in the present work are shown in Table 3. It can be seen that the decreasing tendency of calculated lattice parameter is similar to the analytical results of XRD spectrum. It is easy to be seen that V addition reduces the lattice parameters of the alloy. The phenomenon should be attributed to existg atomic size difference.

In summary, NbMoTaW and NbMoTaWV RHEA are single-phase BCC solid solution based on the analysis of empirical criterions, formation enthalpy, cohesive energy and XRD spectrum. Therefore, BCC NbMoTaWV RHEA supercell model was adopted to calculate the elastic properties and electronic structure.

4.2. Elastic properties

Table 4 shows nine elastic constants of optimized NbMoTaW and NbMoTaWV RHEA. Generally, the crystals with body centered cubic structure have three independent elastic constants. There are nine independent elastic constants in the supercell model we adopted. Therefore, we took the average value of the elastic constants obtained by SQS model in order to reduce the influence of SQS model's low symmetry and large size [24,25]. The results of calculated average value of the elastic constants shown in Table 5, which were described as formula (3):

$$C_{11} = \frac{C'_{11} + C'_{22} + C'_{33}}{3}; C_{12} = \frac{C'_{12} + C'_{23} + C'_{13}}{3}; C_{44} = \frac{C'_{44} + C'_{55} + C'_{66}}{3} \quad (3)$$

Table 1
The formation enthalpy (E_{form}), cohesive energy (E_{coh}) and the total energy (E_{tot}) of NbMoTaWV RHEA for the optimized SQS model.

alloy	Crystal structure	number of atoms in a crystal cell	E_{tot} (eV)	H_{form} (eV/atom)	E_{coh} (eV/atom)
NbMoTaWV	BCC	10	−1756.8780	−0.092	−7.346
	FCC	20	−3503.7878	0.406	−6.847
	HCP	10	−1750.3230	0.563	−6.690

Table 2
The total energy (E_{solid}) of a single crystal cell for every component in NbMoTaWV RHEA and total energy (E_{atom}) of individual atom in a corresponding single crystal cell.

components	Nb	Mo	Ta	W	V
E_{solid} (eV)	−285.0977	−440.8225	−279.6026	−425.0647	−325.3658
E_{atom} (eV)	−133.8006	−214.2942	−131.5383	−203.8927	−158.1854

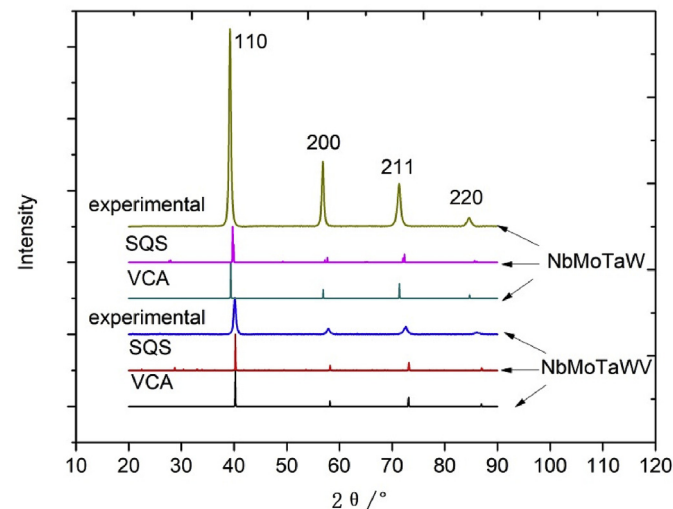


Fig. 2. The calculated and experimental XRD spectrum of NbMoTaW and NbMoTaWV RHEA.

According to Born Rule [16], formula (4) is identified as the decisive condition of mechanical stability:

$$C_{11} > 0, C_{44} > 0, (C_{11} - C_{12}) > 0, C_{11} + 2C_{12} > 0 \quad (4)$$

On the basis of the calculated data, we draw a conclusion that NbMoTaW and NbMoTaWV RHEA were of mechanical stability.

Table 5 shows the mean elastic constants (C_{11} , C_{12} , C_{44}), Cauchy pressure ($C_{12} - C_{44}$), bulk modulus (B), shear modulus (G), Young's modulus (E), and poisson's ratio (ν) of NbMoTaW and NbMoTaWV RHEA. The polycrystal elastic modulus obtained using the Voigt-Reuss-Hill (VRH) method [26]. From the data in Tables 4 and 5, the elastic constants and polycrystalline elastic modulus of those RHEAs were calculated using the VCA and SQS methods. The calculated values of elastic constants and polycrystalline elastic

Table 3
Lattice parameters of optimized NbMoTaW and NbMoTaWV RHEA.

alloys	lattice parameters	this work (VCA method)	this work (SQS method)	experimental values [9,19]	theoretical values [18]
NbMoTaW	a	3.195	3.193	3.213	3.271
	b	3.195	3.193	3.213	3.271
	c	3.195	6.432	3.213	3.271
NbMoTaWV	a	3.167	3.165	3.185	—
	b	3.167	3.165	3.185	—
	c	3.167	15.830	3.185	—

Table 4
Nine independent elastic constants in the supercell model of optimized NbMoTaW and NbMoTaWV RHEA.

alloys	C'_{11}	C'_{12}	C'_{13}	C'_{22}	C'_{23}	C'_{33}	C'_{44}	C'_{55}	C'_{66}	data sources
NbMoTaW	401	166	154	400	154	375	76	76	85	¹
	330	194	181	320	194	349	96	78	93	³
NbMoTaWV	386	141	145	386	144	365	65	64	65	²

^{1,2}calculated rkesults from VCA and SQS method in the present work;³theoretical value [27].

modulus decrease after V addition into NbMoTaW RHEA. In addition, it is easy to build models with fast calculating speed using the VCA method, while the SQS model is complex and time-consuming.

The influence of V addition on the brittle-ductility of NbMoTaW HEA is usually judged by the ratio of shear modulus to bulk modulus (G/B). If $G/B < 0.57$, it shows ductility, and the smaller the G/B is, the better the ductility is. Otherwise, it exhibits brittle behavior [26]. The calculated G/B values of NbMoTaW and NbMoTaWV RHEA are listed in Table 5. It can be seen that the G/B value of NbMoTaW (VCA: 0.413 and SQS: 0.390) and NbMoTaWV (VCA: 0.398 and SQS: 0.369) are basically same, indicating that both the alloys have similar ductility. The above information is well agreed with the nearly same compressing strain of NbMoTaWV (1.9%) and NbMoTaW RHEAs (1.7%) tested by Senkov [11]. Normally, Cauchy pressure ($C_{12} - C_{44}$) is often used to evaluate the bonding characteristics of the alloy. If the ($C_{12} - C_{44}$) is positive, the metal bond will be formed, otherwise, the covalent bond will be formed. Cauchy pressure of the two alloys are shown in Table 5. All the values of ($C_{12} - C_{44}$) are positive, indicating that the atoms in the alloys are bonded by metal bonds.

Hardness can reflect the comprehensive mechanical properties of materials. Thus, hardness of the NbMoTaWV and NbMoTaW RHEAs were calculated to investigate the effect of V addition on the mechanical properties of NbMoTaW RHEA. Generally, microhardness (H_v) of alloys can be predicted through calculated bulk modulus and shear modulus according to formula (5):

$$H_v = \left(2 \times \left(\frac{G^3}{B^2} \right)^{0.585} \right) - 3 \quad (5)$$

The predicted and experimental hardness of NbMoTaW and NbMoTaWV RHEA are shown in Fig. 3. It can be seen that V addition has a little improvement on the hardness of NbMoTaW RHEA. Obviously, the predicted hardness values of the alloy are well consistent with the experimental values [21]. Compared with the

Table 5

The mean elastic constants (C_{ij} /GPa), Cauchy pressure ($C_{12}-C_{44}$ /GPa), bulk modulus (B/GPa), shear modulus (G/GPa), Young's modulus (E/GPa) and poisson's ratio(ν) of NbMoTaW and NbMoTaWV RHEA.

RHEAs	C_{11}	C_{12}	C_{44}	$C_{12}-C_{44}$	B	G	G/B	E	ν	methods
NbMoTaW	425	158	86	72	247	102	0.413	270	0.318	VCA
	392	158	79	79	236	92	0.390	245	0.327	SQS
NbMoTaWV	421	144	72	72	236	94	0.398	249	0.325	VCA
	379	143	65	78	222	82	0.369	200	0.348	SQS

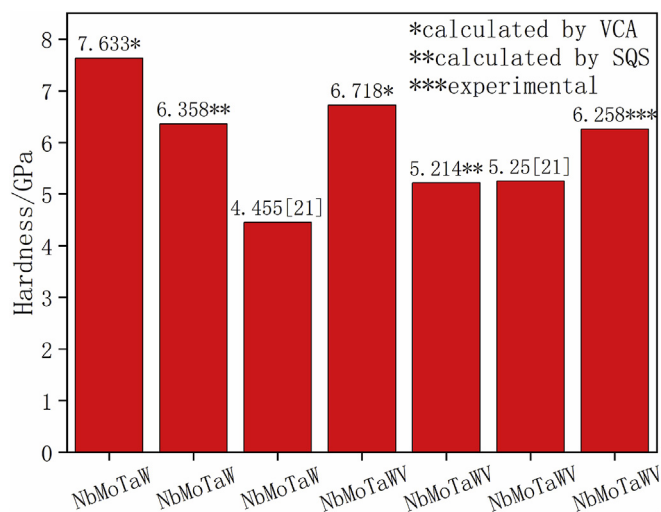


Fig. 3. The calculated and experimental microhardness of NbMoTaW and NbMoTaWV RHEA.

experimental value of 5.250 GPa [21], the predicted hardness of NbMoTaWV RHEA is 5.214 GPa in the present work. The deviation is only 0.69%, which demonstrates that the special quasi-random supercell method combined with the first principle based on density functional theory is feasible to predict the elastic constants, polycrystalline modulus and hardness of disordered high-entropy alloys.

4.3. Electronic structure

Fig. 4 shows the energy band structure of NbMoTaW and NbMoTaWV RHEA along with the highly symmetric direction of Brillouin region. The red dotted line in the figure represents the position of Fermi energy level. The energy band structure near the Fermi level is closely related to the material properties. As shown in Fig. 4 (a) and (b), the energy gap is zero due to the overlap between conduction band and valence band, which demonstrates that both RHEAs show metal characteristics. Compared with NbMoTaW RHEA, NbMoTaWV RHEA has a compacted energy band, which may be attributed to the strong interaction of orbital electrons between V atom and other four atoms. The energy band overlapping increases significantly after V addition into NbMoTaW RHEA, indicating that V addition enhances the bonding strength of the alloy system.

Fig. 5 shows the total and partial densities of states of NbMoTaW and NbMoTaWV RHEA. It can be seen that there is no significant difference in the total density of states between NbMoTaW and NbMoTaWV RHEA, indicating that V addition makes the phase structure of NbMoTaW alloy stable. There is no phase transition in NbMoTaW RHEA after V addition. One difference is that V addition makes the strong peak sharper and closer to the Fermi energy level. Another change is that the conduction band in high energy region

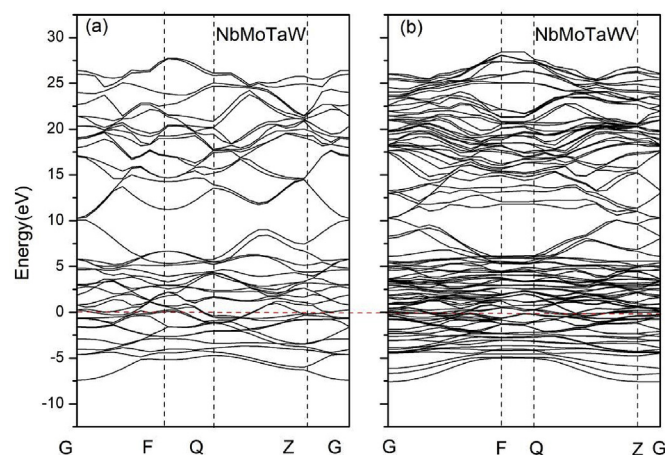


Fig. 4. Energy band structure of RHEAs: (a) NbMoTaW; (b) NbMoTaWV.

becomes flatter and more compact, indicating that strong interaction of orbital electrons after V addition into NbMoTaW RHEA and V addition makes the bonds combine sufficiently. The strong peak energies near the Fermi energy level of NbMoTaW RHEA are -2.36eV and 2.69eV and NbMoTaWV RHEA are -0.802eV and 3.12eV . That is to say, the pseudo-energy gaps of NbMoTaW and NbMoTaWV RHEA are 5.05eV and 3.922eV , respectively. The pseudo-energy gap, which is defined as the energy difference between two strong peaks near the Fermi energy level, reflecting the covalency of the alloy system. The wider the pseudo-energy gap is, the stronger the covalency of the system is [28,29]. The calculated results are that V addition makes the valence band closer to Fermi level apparently and the conduction band flatter and more compact, shortening the pseudo-energy gap in quaternary RHEA. That is to say, the number of covalent bonds among Nb, Mo, Ta, W atoms decrease after V addition into NbMoTaW alloy, which may lead to the increasing of metallic bonding. It is thought to enhance the bonding strength and improve NbMoTaW RHEA's mechanical properties. The analytical consequence is well consistent with the results judged by Cauchy stress and energy bonds. In addition, the total density of states of NbMoTaWV RHEA is far more than that of NbMoTaW RHEA, indicating that NbMoTaWV has stronger metallic properties than NbMoTaW.

In order to further understand the contribution of electrons of each element to the total density of states of the alloy, the partial density of states of each element of NbMoTaW and NbMoTaWV RHEA was calculated and is shown in Fig. 5. It is obvious that the valence band near the Fermi energy level of NbMoTaW alloy, with a high overlap rate, is formed after hybridization of d-orbital electron of Nb, Mo, Ta and W. There are a few contribution originated from s-orbital electron of Nb, Mo, Ta and W atoms. The conduction band of NbMoTaWV alloy is formed after the hybridization of d-orbital and p-orbital electron among Nb, Mo, Ta, W and V atoms. Compared with the partial density of states of NbMoTaW RHEA, the conduction band with less peak valley in high energy region of NbMoTaWV

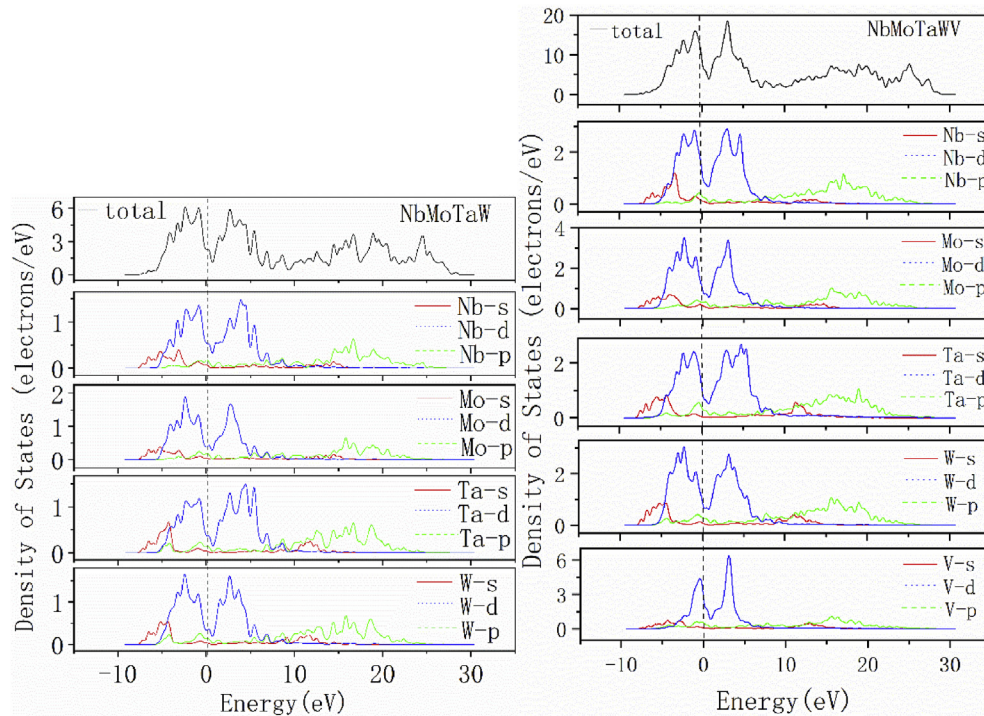


Fig. 5. The total and partial density of states of NbMoTaW and NbMoTaWV RHEA.

RHEA becomes more compact, meaning that the interactions in atoms become stronger.

Fig. 6 shows the charge density and charge density difference diagram of NbMoTaW and NbMoTaWV RHEA along the crystal plane (110), which can directly reflect the bonding and charge transfer between atoms. As shown in Fig. 6 (a) and (b), the electron cloud distributes uniformly around Nb, Mo, Ta and W atoms without obvious directionality, which verifies the formation of metal bonds [30]. It is obvious that the overlap of the electron cloud between Mo and W become stronger and take place stronger electron interaction after V addition. Fig. 5 (c) and (d) are the charge density difference diagrams. The red means losing electrons and the blue represents getting electrons. It is easy to be seen that the red around V atom is brighter than other atoms, indicating that V atom loses electrons and the interaction of orbitals electrons

between V atom and Nb, Mo, Ta and W is stronger than that among Nb, Mo, Ta and W. This may be the reason why the formed covalent bonds between Nb, Mo, Ta and W decrease and the metal bonds increase.

5. Conclusion

VCA and SQS models based on first-principle calculation were used to calculate the phase structure, mechanical properties and electronic structure of NbMoTaW and NbMoTaWV RHEA. The calculated E_{form} , E_{coh} , and XRD spectrum indicate that both RHEAs were single-phase BCC solid solution. According to the calculated electronic structures, V addition enhanced the bonding strength and improved mechanical properties of NbMoTaW RHEA. Both NbMoTaW and NbMoTaWV RHEA exhibited metal characteristics.

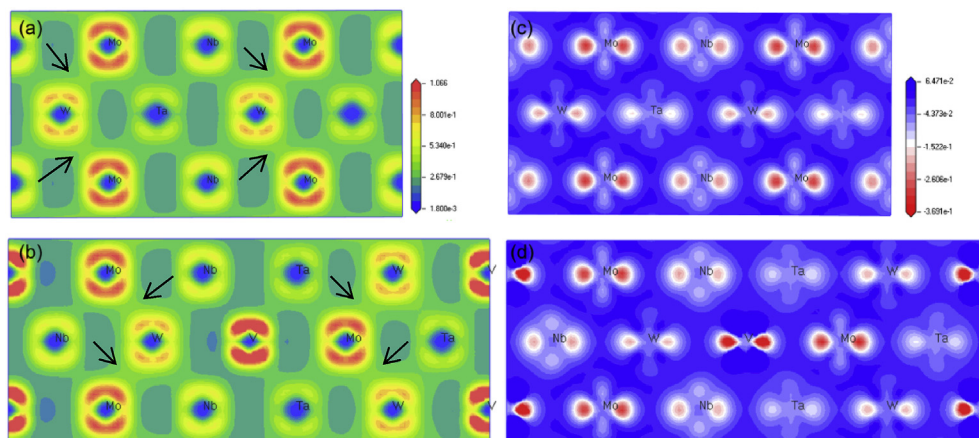


Fig. 6. (a) The charge density diagram of NbMoTaW RHEA. (b) The charge density diagram of NbMoTaWV RHEA. (c) The charge density difference diagram of NbMoTaW RHEA. (d) The charge density difference diagram of NbMoTaWV.

The calculated results and the experimental data are coincident, indicating that first-principle calculation is an effective method to simulate and predict the properties of RHEA. This provides an approach to investigate the alloying enhancement of RHEAs and other alloys.

Credit author statement

Y.L. Hu, L.H. Bai and Y.G. Tong contributed the central idea, analyzed most of the data, and wrote the initial draft of the paper. The remaining authors contributed to refining the ideas, carrying out additional analyses and finalizing this paper.

Declaration of competing interest

The authors declare that they have no known competing financial interests or personal relationships that could have appeared to influence the work reported in this paper.

Acknowledgments

This work was supported by National Key R&D Program of China (No. 2018YFC1902401), Natural Science Foundation of Hunan Province of China (No. 2019JJ50657), Hunan Key R&D Project (No. 2019kj001), Educational Commission of Hunan Province of China (No. 18C0210) and the “Double First-Class” Scientific Research International Cooperation and Development Project of Changsha University of Science and Technology.

References

- [1] J.W. Yeh, S.K. Chen, S.J. Lin, J.Y. Gan, T.S. Chin, T.T. Shun, C.H. Tsau, S.Y. Chang, Nanostructured high-entropy alloys with multiple principal elements: novel alloy design concepts and outcomes, *Adv. Eng. Mater.* 6 (2004) 299–303, <https://doi.org/10.1002/adem.200300567>.
- [2] X.W. Qiu, Y.P. Zhang, C.G. Liu, Effect of Ti content on structure and properties of $\text{Al}_2\text{CrFeNiCoCuTi}_x$ high-entropy alloy coatings, *J. Alloys Compd.* 585 (2014) 282–286, <https://doi.org/10.1016/j.jallcom.2013.09.083>.
- [3] F. Otto, A. Dlouhý, Ch Somsen, H. Bei, G. Eggeler, E.P. George, The influences of temperature and microstructure on the tensile properties of a CoCrFeMnNi high-entropy alloy, *Acta Mater.* 61 (2013) 5743–5755, <https://doi.org/10.1016/j.actamat.2013.06.018>.
- [4] Q. Fang, Y. Chen, J. Li, Y. Liu, Y. Liu, Microstructure and mechanical properties of FeCoCrNiNb_x high-entropy alloy coatings, *Phys. Rev. B Condens. Matter* 550 (2018) 112–116, <https://doi.org/10.1016/j.physb.2018.08.044>.
- [5] B. Wang, X. Yao, C. Wang, X. Zhang, X. Huang, Mechanical properties and microstructure of a NiCrFeCoMn high-entropy alloy deformed at high strain rates, *Entropy* 20 (2018) 892, <https://doi.org/10.3390/e20110892>.
- [6] Y.G. Tong, P.B. Qi, X.B. Liang, Y.X. Chen, Y.L. Hu, Z.F. Hu, Different-shaped ultrafine MoNbTaW HEA powders prepared via mechanical alloying, *Materials* 11 (2018) 1250, <https://doi.org/10.3390/ma11071250>.
- [7] J.A. Smeltzer, C.J. Marvel, B.C. Hornbuckle, A.J. Roberts, J.M. Marsico, A.K. Giri, K.A. Darling, J.M. Rickman, H.M. Chan, M.P. Harmer, Achieving ultra hard refractory multi-principal element alloys via mechanical alloying, *Mater. Sci. Eng., A* 763 (2019) 138140, <https://doi.org/10.1016/j.msea.2019.138140>.
- [8] H.P. Wang, P. Lü, X. Cai, B. Zhai, J.F. Zhao, B. Wei, Rapid solidification kinetics and mechanical property characteristics of Ni–Zr eutectic alloys processed under electromagnetic levitation state, *Mater. Sci. Eng., A* 772 (2020) 138660, <https://doi.org/10.1016/j.msea.2019.138660>.
- [9] J. Wu, C. Li, Y. Liu, Y. Wu, Q. Guo, H. Li, H. Wang, Effect of annealing treatment on microstructure evolution and creep behavior of a multiphase Ni3Al-based superalloy, *Mater. Sci. Eng., A* 743 (2019) 623–635, <https://doi.org/10.1016/j.msea.2018.11.126>.
- [10] Z.D. Han, H.W. Luan, X. Liu, N. Chen, X.Y. Li, Y. Shao, K.F. Yao, Microstructures and mechanical properties of $\text{Ti}_x\text{NbMoTaW}$ refractory high-entropy alloys, *Mater. Sci. Eng.* 712 (2018) 380–385, <https://doi.org/10.1016/j.msea.2017.12.004>.
- [11] O.N. Senkov, G.B. Wilks, J.M. Scott, D.B. Miracle, Mechanical properties of $\text{Nb}_{25}\text{Mo}_{25}\text{Ta}_{25}\text{W}_{25}$ and $\text{V}_{20}\text{Nb}_{20}\text{Mo}_{20}\text{Ta}_{20}\text{W}_{20}$ refractory high entropy alloys, *Intermetallics* 19 (2011) 698–706, <https://doi.org/10.1016/j.intermet.2011.01.004>.
- [12] W.R. Wang, W.L. Wang, S.C. Wang, Y.C. Tsai, C.H. Lai, J.W. Yeh, Effects of Al addition on the microstructure and mechanical property of $\text{Al}_x\text{CoCrFeNi}$ high-entropy alloys, *Intermetallics* 26 (2012) 44–51, <https://doi.org/10.1016/j.intermet.2012.03.005>.
- [13] G.A. Salishchev, M.A. Tikhonovsky, D.G. Shaysultanov, N.D. Stepanov, A.V. Kuznetsov, I.V. Kolodiy, A.S. Tortika, O.N. Senkov, Effect of Mn and V on structure and mechanical properties of high-entropy alloys based on CoCrFeNi system, *J. Alloys Compd.* 591 (2014) 11–21, <https://doi.org/10.1016/j.jallcom.2013.12.210>.
- [14] S.W. Xin, M. Zhang, T.T. Yang, Y.Y. Zhao, B.R. Sun, T.D. Shen, Ultrahard bulk nanocrystalline VNbMoTaW high-entropy alloy, *J. Alloys Compd.* 769 (2018) 597–604, <https://doi.org/10.1016/j.jallcom.2018.07.331>.
- [15] F.Y. Tian, A review of solid-solution models of high-entropy alloys based on ab initio calculations, *Front. Mater.* 4 (2017), <https://doi.org/10.3389/fmats.2017.00036>.
- [16] Y.K. Mu, H.X. Liu, Y.H. Liu, X.W. Zhang, Y.H. Jiang, T. Dong, An ab initio and experimental studies of the structure, mechanical parameters and state density on the refractory high-entropy alloy systems, *J. Alloys Compd.* 714 (2017) 668–680, <https://doi.org/10.1016/j.jallcom.2017.04.237>.
- [17] L. Bellaiche, D. Vanderbilt, Virtual crystal approximation revisited: application to dielectric and piezoelectric properties of perovskites, *Phys. Rev. B* 61 (2000) 7877–7882, <https://doi.org/10.1103/PhysRevB.61.7877>.
- [18] M.Q. Liao, Y. Liu, L.J. Min, Z.H. Lai, T.Y. Han, D.N. Yang, J.C. Zhu, Alloying effect on phase stability, elastic and thermodynamic properties of Nb–Ti–V–Zr high entropy alloy, *Intermetallics* 101 (2018) 152–164, <https://doi.org/10.1016/j.intermet.2018.08.003>.
- [19] A. Zunger, S.H. Wei, L.G. Ferreira, J.E. Bernard, Special quasirandom structures, *Phys. Rev. Lett.* 65 (1990) 353–356, <https://doi.org/10.1103/PhysRevLett.65.353>.
- [20] X.Q. Li, First-principles study of the third-order elastic constants and related anharmonic properties in refractory high-entropy alloys, *Acta Mater.* 142 (2018) 29–36, <https://doi.org/10.1016/j.actamat.2017.09.041>.
- [21] O.N. Senkov, G.B. Wilks, D.B. Miracle, C.P. Chuang, P.K. Liaw, Refractory high-entropy alloys, *Intermetallics* 18 (2010) 1758–1765, <https://doi.org/10.1016/j.intermet.2010.05.014>.
- [22] X.J. Yao, X.F. Shi, Y.P. Wang, G.Y. Gan, B.Y. Tang, The mechanical properties of high entropy (–like) alloy $\text{W}_x(\text{TaTiVCr})_{1-x}$ via first-principles calculations, *Fusion Eng. Des.* 137 (2018) 35–42, <https://doi.org/10.1016/j.fusengdes.2018.08.008>.
- [23] Z.S. Nong, J.C. Zhu, R.D. Zhao, Prediction of structure and elastic properties of AlCrFeNiTi system high entropy alloys, *Intermetallics* 86 (2017) 134–146, <https://doi.org/10.1016/j.intermet.2017.03.014>.
- [24] Z.Q. Wen, Y.H. Zhao, J.Z. Tian, S. Wang, Q.W. Guo, H. Hou, Computation of stability, elasticity and thermodynamics in equiatomic AlCrFeNi medium-entropy alloys, *J. Mater. Sci.* 54 (2019) 2566–2576, <https://doi.org/10.1007/s10853-018-2943-7>.
- [25] Z. Lu, Z. Lei, H. Huang, S. Liu, F. Zhang, D. Duan, P. Cao, Y. Wu, X. Liu, H. Wang, Deformation behavior and toughening of high-entropy alloys, *Acta Metall. Sin.* 54 (2018) 1153–1166, <https://doi.org/10.11900/0412.1961.2018.00372>.
- [26] J. Zhang, Y.N. Huang, C. Mao, P. Peng, Structural, elastic and electronic properties of θ (Al_2Cu) and δ (Al_2CuMg) strengthening precipitates in Al–Cu–Mg series alloys: first-principles calculations, *Solid State Commun.* 152 (2012) 2100–2104, <https://doi.org/10.1016/j.ssc.2012.09.003>.
- [27] Y. Wu, Microstructure and Toughening Mechanism of Ti–Zr–Nb Refractory High Entropy Alloy, University of Science and Technology Beijing, 2019.
- [28] Y. Wang, J. He, M. Yan, C. Li, L. Wang, Y. Zhou, First-principles study of NiAl alloyed with rare earth element Ce, *J. Mater. Sci. Technol.* 27 (2011) 719–724, [https://doi.org/10.1016/S1005-0302\(11\)60132-1](https://doi.org/10.1016/S1005-0302(11)60132-1).
- [29] Z.N. Ma, J. Min, W. Lei, First-principles study of electronic structures and phase stabilities of ternary intermetallic compounds in the Mg–Y–Zn alloys, *Acta Phys Sin-ch Ed.* 64 (2015) 1026–1031, <https://doi.org/10.7498/aps.64.187102>.
- [30] J. Zhang, Q. Xu, Y. Hu, C. Mao, X. Zhou, X. Lu, M. Zhang, Y. Tong, K. Tang, P. Peng, Interfacial bonding mechanism and adhesive transfer of brazed diamond with Ni-based filler alloy: first-principles and experimental perspective, *Carbon* 153 (2019) 104–115, <https://doi.org/10.1016/j.carbon.2019.07.015>.